

# Stochastic Sampling of Operator Growth Dynamics

Ayush De,<sup>1</sup> Umberto Borla,<sup>1</sup> Xiangyu Cao,<sup>2</sup> and Snir Gazit<sup>1,3</sup>

<sup>1</sup>*Racah Institute of Physics, The Hebrew University of Jerusalem, Jerusalem 91904, Israel*

<sup>2</sup>*Laboratoire de Physique de l'École normale supérieure, ENS, Université PSL, CNRS, Sorbonne Université, Université Paris Cité, F-75005 Paris, France*

<sup>3</sup>*The Fritz Haber Research Center for Molecular Dynamics, The Hebrew University of Jerusalem, Jerusalem 91904, Israel*

(Dated: January 15, 2024)

We put forward a Monte Carlo algorithm which samples the Euclidean time operator growth dynamics at infinite temperature. Crucially, our approach is free of the numerical sign problem for a range of quantum many-body spin systems, allowing for numerically exact and unbiased calculations. We apply this methodological headway to study the high-frequency dynamics of the mixed-field quantum Ising model (QIM) at one and two dimensions. Our results corroborate the recently proposed operator growth hypothesis, predicting an exponential fall-off of generic response functions at large frequencies. Remarkably, our calculations are sufficiently sensitive to detect subtle logarithmic corrections of the hypothesis in one dimension. In addition, in two dimensions, we uncover a non-trivial crossover between two large frequency decay rates. Lastly, we find that the growth rate of the operator support size is dominated by boundary effects, with a logarithmic correction in one dimension.

*Introduction* — Within the Heisenberg representation of quantum mechanics, the time evolution of operators is governed by their commutation relations with the Hamiltonian. Under generic many-body dynamics, local operators are expected to evolve into increasingly complex and non-local operator strings. This process of “operator growth” is equivalent to the scrambling of quantum information in complex systems, and closely related to quantum chaos. As such, understanding the precise properties of operator growth is a fundamental line of research that has driven a great amount of theoretical and experimental work [1–9]. It has direct links to the question of how the laws of quantum mechanics bring about thermalization or its failure in isolated systems [10–14]. It is also a useful tool for investigating the fate of information in a black hole and how to retrieve it [15–19].

In this context, an interesting way to quantify the rate of operator growth, besides the much studied out-of-time order correlator, is to examine the high-frequency regime of the spectral density associated with generic correlators [20]. Recently, Ref. [21] proposed an operator growth hypothesis that translates to an exponentially decaying large frequency tail

$$\Phi(\omega) \sim \exp(-|\omega|/\omega_0) \quad (1)$$

in generic many-body systems with finite local bandwidth. The energy scale  $\omega_0$  provides an upper bound to the Lyapunov exponent of out-of-time order correlators [21–23], and is thus an alternative measure of operator growth [24–30]. Crucially, this quantity is experimentally accessible [31], e.g., from the pre-thermalization time in a fast periodic drive [32].

Testing the operator growth hypothesis in concrete lattice models is particularly challenging due to the inherent difficulty of simulating many-body quantum dynamics

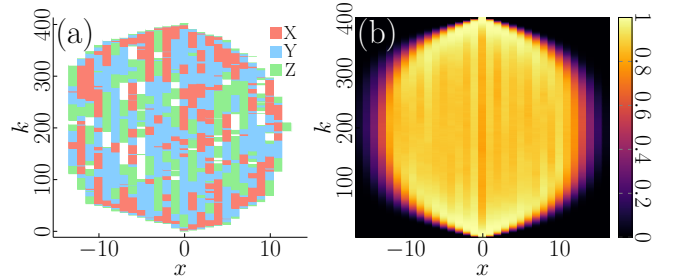


FIG. 1: (a) A space-time snapshot of the Euclidean time operator growth process extracted from the 400<sup>th</sup> moment of the Pauli  $Z$  operator at site 0 of the 1D mixed field QIM. Transformations are generated by Liouvillians between time slices (indexed by  $k$ ). The colors correspond to the different Pauli operators. (b) The average occupation probability on a site by a non-identity Pauli operator resulting from operator growth arising from the same Monte Carlo dynamics as (a).

with classical resources. Direct evidence for the hypothesis is largely limited to large- $N$  or semi-classical models [20, 23, 30, 33, 34] and brute-force numerics of small to intermediate system sizes that suffer from sizable finite size effects [35]. Although analytical bounds supporting the conjecture have been obtained for finite-dimensional systems [36, 37], these results are not satisfactory in that they do not provide an accurate estimate of  $\omega_0$  or the precise functional form of the spectral function. It is, therefore, desirable to devise efficient numerical schemes that can reliably test the operator growth hypothesis.

In this Letter, we present a Monte Carlo method that samples the Euclidean time operator growth dynamics at infinite temperature in an unbiased and statistically exact manner. The Monte Carlo method tracks the Euclidean time evolution of *operators* (Fig. 1a) instead of

the standard wave function approach that is common in conventional quantum Monte Carlo calculations. Crucially, our scheme does not suffer from the notorious numerical sign problem when applied to a broad family of lattice spin models of interest. We employ our method to study the mixed-field QIM in both one and two dimensions. Our results provide high-precision tests of the hypothesis. In particular, we pinpoint the subtle log-correction to Eq. (1) in one dimension, and unveil an intriguing crossover between two high-frequency tails in two dimensions. Finally, we determine the dynamical scaling properties of the operator support size.

*Operator-space partition function* — In statistical physics, Monte Carlo schemes aim to sample from a partition function representing a weighted sum over the configuration space. In our case, the relevant partition function is the auto-correlation function of a local operator,  $O$ , analytically continued to imaginary time:

$$\mathcal{Z}(\tau) := \langle O | e^{\mathcal{L}\tau} O \rangle. \quad (2)$$

Here,  $\mathcal{L}O = [H, O]$  is the Liouvillian super operator representing the commutation with the Hamiltonian  $H$ , and  $\langle A | B \rangle = \text{Tr}[A^\dagger B] / \text{Tr}[1]$  denotes the infinite-temperature scalar product on operator space. We shall also assume that  $O$  equals a product of one-site operators. To make contact with the real frequency spectral density (and especially its large frequency tails), it is useful to consider the Taylor expansion of  $\mathcal{Z}(\tau)$  at  $\tau = 0$ :

$$\mathcal{Z}(\tau) = \sum_{n=0}^{\infty} \mu_{2n} \frac{\tau^{2n}}{(2n)!} \quad (3)$$

$$\mu_{2n} = \langle O | \mathcal{L}^{2n} | O \rangle = \int \Phi(\omega) \omega^{2n} \frac{d\omega}{2\pi}. \quad (4)$$

In the last equation, we identify the Taylor expansion coefficients  $\{\mu_{2n}\}$  with the moments of the spectral function  $\Phi(\omega)$ , which follows from a Fourier transform of the analytic continuation to real-time correlators,  $\mathcal{C}(t) = \mathcal{Z}(\tau = it)$ . Thus, high moments encode information about the high-frequency tail of  $\Phi(\omega)$ . In particular, an exponential tail (Eq. (1)) yields:

$$\mu_{2n} \simeq \left( \frac{2n\omega_0}{e} \right)^{2n} \quad (5)$$

for large  $n$ . We recall that the moments grow rapidly, such that  $\mathcal{Z}(\tau)$  converges only when  $\tau < \tau_* = 1/\omega_0$ , and has a pole at  $\tau_*$ .

To evaluate the moments via stochastic sampling, we express  $\mu_{2n}$  as a sum over paths in operator space. Assuming local dynamics, we write  $\mathcal{L} = \sum_{i,a} \mathcal{L}_{i,a}$ , with  $\{\mathcal{L}_{i,a}\}$  denoting local Liouvillian of type  $a$  acting on site  $i$ , as dictated by the underlying Hamiltonian,  $H = \sum_{i,a} H_{i,a}$ , with  $\mathcal{L}_{i,a}O = [H_{i,a}, O]$ . Following the above definitions, we expand the product  $\langle O | \mathcal{L}^{2n} | O \rangle$ , by intro-

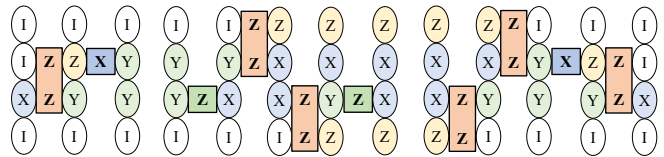


FIG. 2: A typical configuration contributing to the 4-th moment with the horizontal and vertical axes being temporal and spatial respectively. The sites are populated by the  $X$ ,  $Y$ , and  $Z$  Pauli operators or the  $I$  (identity) operator. The temporal direction is generated by the Liouvillians of type  $\mathcal{L}_Z$ ,  $\mathcal{L}_{ZZ}$  and  $\mathcal{L}_X$  corresponding to the three types of local Hamiltonian terms. The empty Liouvillian slots correspond to null superoperators.

ducing operator space resolution of identities between individual Liouvillians:

$$\mu_{2n} = \sum_{\mathcal{S}_{2n}} \prod_{k=0}^{2n-1} \underbrace{(O_{k+1} | \mathcal{L}_{i_k, a_k} O_k)}_{W_{\mathcal{S}_{2n}}}, \quad (6)$$

where the sum is over all local Liouvillian sequences, specified by  $2n$  position-type pairs,  $\mathcal{S}_{2n} = \{(i_k, a_k)\}_{k=0}^{2n-1}$ , with nonzero weight  $W_{\mathcal{S}_{2n}} \neq 0$ . This construction implicitly defines operator histories ( $O_0 = O, O_1, \dots, O_{2n} = O_0$ ) and is reminiscent of the Stochastic Series Expansion (SSE) [38, 39]. We emphasize that, unlike standard quantum Monte Carlo approaches, here, the configuration space is defined via the space of local operators, and transitions between them are generated by the Liouvillian.

The weights  $W_{\mathcal{S}}$  are generally non-positive and can lead to a sign problem, even in cases where the associated Hamiltonian problem is sign problem free. Remarkably, for a class of nontrivial models, the sum in Eq. (6) contains strictly non-negative real terms,  $W_{\mathcal{S}} \geq 0$  [37]. This class includes the mixed-field QIM, with the Hamiltonian,

$$H = -J \sum_{\langle i, j \rangle} Z_i Z_j - \sum_i (h^Z Z_i + h^X X_i). \quad (7)$$

Here,  $\langle i, j \rangle$  define nearest neighbours on a hypercubic lattice, and  $X_i, Z_i$  are the Pauli operators act on sites  $i$  along the  $x, z$  spin axes, respectively. In what follows, we will focus on the numerical study of the mixed field QIM with positive and uniform  $J, h^Z, h^X$ .

*Numerical methods and observables* — Following the expansion of  $\mathcal{Z}(\tau)$  in Eq. (3), we now turn to devise a Monte Carlo algorithm to numerically estimate the moments  $\mu_{2n}$ . To that end, we set  $\tau = 1/J$  in Eq. (2) and restrict the expansion order to obey  $2n \leq 2n_{\max}$ . Analogously to SSE, we consider Liouvillian sequences,  $\mathcal{S}_{2n_{\max}}$ , of fixed length  $2n_{\max}$ , which for an expansion order  $n$  include additional  $(2n_{\max} - 2n)$  factors of the null super-operator  $\mathcal{L}_{0,0} \equiv I$ .

We note that the above truncation is natural in the context of imaginary time Hamiltonian dynamics via SSE simulations. There, for given values of microscopic parameters and temperature, the probability distribution of the expansion order rapidly decays away from its mean value. By contrast, here, we will be interested in targeting *all* moments  $\mu_{2n}$  for  $2n \leq 2n_{\max}$ . As will become clearer below, this entails visiting each expansion order at roughly equal frequency.

The resulting partition function has the following form,

$$G = \sum_{S_{2n_{\max}}} \frac{1}{J^{2n}(2n)!} \quad (8)$$

$$\times \frac{(2n_{\max} - 2n)!(2n)!}{(2n_{\max})!} \prod_{k=0}^{2n_{\max}-1} \langle O_{k+1} | \mathcal{L}_{i_k, a_k} | O_k \rangle,$$

where the combinatorial factors arise from the redundancy in the assignment of null operators. Eq. (8) has a natural diagrammatic interpretation as a sum over  $D = d + 1$  dimensional space-time configurations consisting of on-site Pauli operator, with the dynamics generated by insertions of local Liouvillian super-operators, transitioning between Pauli strings, see Fig. 2.

In the following, we present a set of local Monte Carlo moves that enable traversing between all allowed configurations: (1) **add-drop** – allows switching between different  $n$  sectors by adding or removing a pair of identical local Liouvillians located on the same sites at two consecutive time slices. (2) **swap** – swaps two commuting Liouvillians at different time slices, without changing the expansion order  $n$ . This move is proposed only if there are no non-commuting Liouvillians at intermediate time slices. (3) **interact** – here, two temporally consecutive  $\mathcal{L}_{ZZ}$  Liouvillians that share a single spatial site “interact” to create a pair of temporally consecutive  $\mathcal{L}_Z$  Liouvillians acting on next to nearest neighbour sites. This move allows accessing configurations with an odd number of  $\mathcal{L}_{ZZ}$  and  $\mathcal{L}_Z$  Liouvillians acting on a given site.

In practice, we found it essential to apply a reweighting approach, in the spirit of the Wang-Landau algorithm [40–42], in order to ensure ergodicity due to rapid fall off (or rise) of the expansion order distribution towards large moments. This is achieved by iteratively tuning the relative visiting rate of each expansion order until reaching an approximately uniform distribution across expansion order sectors. In other words, we sample the partition sum  $\mathcal{Z}(\tau)$  near criticality,  $\tau \nearrow \tau_*$ . Additional technical details on the Monte Carlo algorithm are relegated to [43].

Our key physical observable is the moments’ ratio:

$$r_n^2 := \frac{\mu_{2n+2}}{\mu_{2n}} = \frac{\langle \delta_{n', n+1} \rangle_{n'}}{\langle \delta_{n', n} \rangle_{n'}} \times J^2(2n+2)(2n+1). \quad (9)$$

In the above equation, averaging is carried out over the probability distribution of the expansion order  $P(n')$ ,

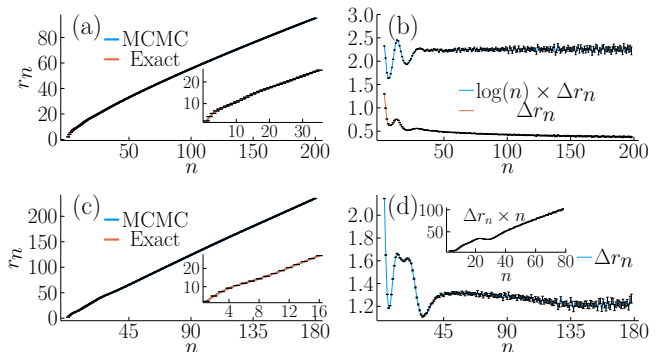


FIG. 3: (a)  $r_n$  vs  $n$  for the  $Z$  operator with  $J = h^Z = h^X = 1$  in 1D. The inset zooms in on the first 35 moments, comparing our calculations with exact brute force numerics. (b)  $\Delta r_n$  vs  $n$  for 1D. This asymptotically falls to zero. Multiplying by  $\log(n)$  recovers a constant plateau. (c) Same as (a) for 2D. The inset has the first 16 moments compared against exact computation. (d)  $\Delta r_n$  vs  $n$  for 2D. Unlike 1D here the log multiplication isn’t needed. The inset shows  $n\Delta r_n$  vs  $n$ .

where the Kronecker delta  $\delta_{n', n}$  counts Monte Carlo events satisfying  $n' = n$ . Effectively,  $r_n^2$  is tied to the ratio between the visiting frequencies of expansion orders  $n + 1$  and  $n$ . The large frequency behavior of Eq. (5), predicts a linear growth of  $r_n$  with  $n$ ,

$$r_n \simeq \frac{2\omega_0 n}{e}. \quad (10)$$

In addition, the prefactor allows a numerical estimation of the decay rate  $\omega_0$ .

To estimate the spatial extent of operator growth, we define the support size at time slice  $k$  as:

$$S_k = \langle \text{Volume}(B_k^d) \rangle. \quad (11)$$

Here,  $B_k^d$  is geometrically defined as the largest region in  $d$  dimensional space enclosed by non-trivial operators at temporal index  $k$ .

*Numerical Results* – In the following, we present Monte Carlo data for the  $Z$  operator dynamics in the mixed field QIM with the microscopic parameters  $h^X = h^Z = J = 1$  in 1D and 2D. We begin our presentation by examining the 1D case. We recall that, due to the restricted dynamics in 1D, the linear growth in Eq. (10) receives a logarithmic correction such that  $r_n \sim n/\log n$  [21, 32, 36, 44, 45]. In Fig. 3a, we depict  $r_n$  as a function of  $n$ . We first note the excellent agreement with brute force calculation (suffering from an unfavourable exponential scaling with the expansion order) as shown in the inset, serving as a non-trivial benchmark of our approach.

Furthermore, we observe that the large  $n$  growth of  $r_n$  deviates from a linear trend. To pin down the source of this deviation and check whether it can be attributed to the aforementioned logarithmic correction in Fig. 3b,

we plot  $\Delta r_n \times \log(n)$ , where  $\Delta r_n$  is a numerical derivative extracted using the five-point stencil method. This quantity is expected to reach a plateau at large  $n$  with the logarithmic correction. Indeed, we find that only in the presence of the log multiplication, the desired plateau is obtained. By contrast,  $\Delta r_n$  asymptotically decays to zero due to the  $1/\log(n)$  factor. We note that this is the first numerically exact confirmation for the predicted log correction associated with the restricted 1D dynamics, as previous brute-force numerics cannot resolve this subtle functional dependence convincingly due to the limited number of accessible moments [21, 35, 46].

We now turn to study 2D systems. In Fig. 3c, we plot the evolution of  $r_n$  with the expansion order  $n$ . As before, we note the precise agreement with brute force computation, shown in the inset. Impressively, the stochastic approach allows access to the first 180 moments, as compared to brute force methods that are limited to the first 16 moments. We observe a clear linear trend of  $r_n$ , which is the first extensive test of the operator growth hypothesis in a concrete model beyond 1D systems.

In Fig. 3d, we plot  $\Delta r_n$ , and remarkably, we find an intriguing two-plateau structure. We infer that the spectral density features a crossover between two exponential tails. Indeed, if we suppose

$$\Phi(\omega) \sim \begin{cases} e^{-|\omega|/\omega_1} & |\omega| \lesssim \omega_c \\ e^{-|\omega|/\omega_2} & |\omega| \gtrsim \omega_c \end{cases} \quad (12)$$

where  $\omega_1$  and  $\omega_2$  are the decay rates and  $\omega_c$  is the crossover scale. Using a saddle point approximation of Eq. (4), we may find that

$$\Delta r_n \approx \begin{cases} 2\omega_1/e & n \lesssim n_1 = \omega_c/2\omega_1 \\ 2\omega_2/e & n \gtrsim n_2 = \omega_c/2\omega_2 \end{cases} \quad (13)$$

In particular, we have  $n_1\omega_1 = n_2\omega_2 = \omega_c/2$ . To show our numerical results are consistent with Eq. (12), we plot  $n\Delta r_n$  in the inset of Fig. 3d, and find a remarkably large  $\omega_c \approx 90J$ . This crossover would have been missed in a brute-force calculation.

Owing to the thermal nature of the dynamics, we expect the large  $n$  behavior of  $r_n$  to be universal for typical local operators with a given set of model parameters. In [43], we indeed see this anticipated behavior for boundary  $X$  operator, with  $\log(n)\Delta r_n \simeq 2.2(1)J$  and  $\Delta r_n \simeq 1.26(4)J$  in 1D and 2D respectively, consistent with the plots here. We also find that the structure of the intermediate plateau as seen in 2D is not universal. Nevertheless, the asymptotic plateau value is reached only at a similar large value  $n_2 \approx 40$ . Correspondingly, the high-frequency tail of the spectral density is truly established only at a frequency that was numerically inaccessible before the present work.

*Statistical mechanics perspective of operator growth* – From the point of view of statistical mechanics, it is nat-

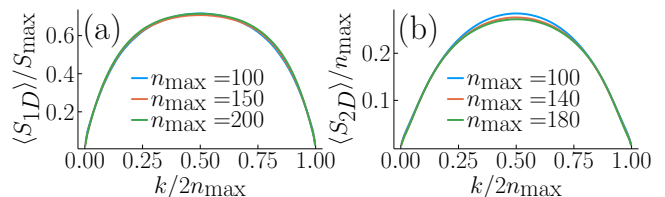


FIG. 4: Scaling collapse of the average operator support size (for the  $Z$  operator), as function of  $k$ , for different values of  $n_{\max}$ , in 1D (a), where  $S_{\max} := n_{\max}/\log n_{\max}$ , and in 2D (b).

ural to examine the geometric properties of the operator string configurations Fig. 1b. In particular, the configurations with large  $n_{\max}$  describe the vicinity of the critical point  $\tau \nearrow \tau_*$  in the partition function (3) (in 1D  $\tau_* = \infty$  because of the log-correction). Therefore, these large  $n_{\max}$  configurations exhibit universal, scale-invariant behavior ubiquitous to continuous phase transitions.

To illustrate this point, we measured the average support size of the operator string as a function of temporal index  $k$  in configurations of an increasing range of maximal expansion order  $n_{\max}$ . The results, plotted in Fig. 4, are in agreement with the following scaling ansatz in the large  $n_{\max}$  limit:

$$\langle S_{2D} \rangle = n_{\max} f_{2D}(k/2n_{\max}), \quad (14a)$$

$$\langle S_{1D} \rangle = \frac{n_{\max}}{\log(n_{\max})} f_{1D}(k/2n_{\max}) \quad (14b)$$

where  $f_{2D}$  and  $f_{1D}$  are scaling functions, which capture the evolution of the operator size growth to an  $n_{\max}$ -dependent maximum (and then decrease) in terms of rescaled time  $k/2n_{\max}$  and size  $S/S_{\max}$ .

The maximal size  $S_{\max} \sim n_{\max}$  in 2D, and we expect the same in higher dimensions as well, since this is the only asymptotics compatible with the universal moment growth in Eq. (5). The slow convergence to the scaling collapse echos the late establishment of the universal growth observed above. In 1D, the maximal size  $S_{\max} = n_{\max}/\log(n_{\max})$  has a log-correction, which has the same geometric origin as the log-correction to the moment growth: in 1D, the operator can only grow at the two extremities, which is a severe entropy penalty. Therefore the dominant contributions must be a compromise: the operator grows less in order to “scramble” more in the bulk. Previous arguments [36, 44] indicated a three-stage process where the operator grows to  $\sim S_{\max}$  at  $k \sim S_{\max}$ , then stays as such until  $2n_{\max} - k \sim S_{\max}$  at which point the operator starts to shrink. In units of rescaled time  $k/2n_{\max}$ , the growth and shrinking stages’ duration would be vanishing  $\sim 1/\log(n_{\max})$ , and the scaling function  $f_{1D}$  would be a constant. In Fig. 4 we see indeed that a plateau establishes itself and extends to the whole interval as  $n_{\max}$  increases, however very slowly (due to the log dependence). In 2D, one may worry that a

similar “boundary-versus-bulk” entropy penalty applies as well. However, delicate rigorous arguments confirm that this is not the case [36]. Put simply, these arguments state that the operator support in 2D can have a “rough” boundary (with length comparable to the bulk area) and thus enough ways to grow in order to generate the moment asymptotics (5). Our results on moment ratio asymptotics provide strong (yet indirect) evidence of this unexpected geometric fact, whose direct observation will require pushing the numerics to large  $n$ .

*Discussion* – We conclude our presentation by flagging several research directions motivated by our results. Our approach can be extended to models whose associated Liouvillian dynamics are expressed as sign problem-free sums. The quantum XY model is a notable example [37], which crucially admits a global U(1) symmetry and hence can provide access to transport properties of conserved charges [47, 48]. The presence of disorder is also compatible with our method, it will be interesting to investigate the signature of Many-Body Localization in the evolution of operator strings. Another important direction is extracting real frequency dynamical spectral functions away from the high-frequency limit, as can, in principle, be via Lanczos coefficients expressed in terms of moment ratios [49–51]. We note that the latter might suffer from high sensitivity to statistical noise and may require an improvement on current algorithms. Lastly, we expect the support size scaling functions to be universal and valid for a generic class of chaotic Hamiltonians, and predicting them theoretically is an interesting open question. We leave the aforementioned possibilities to future efforts.

*Acknowledgements* – We thank Ehud Altman and Assa Auerbach for fruitful discussions. S.G. acknowledges support from the Israel Science Foundation (ISF) Grant no. 586/22 and the US–Israel Binational Science Foundation (BSF) Grant no. 2020. U.B. acknowledges support from the Israel Academy of Sciences and Humanities through the Excellence Fellowship for International Postdoctoral Researchers. Computational resources were provided by the Intel Labs Academic Compute Environment and the Fritz Haber Center for Molecular Dynamics, Hebrew University.

---

[1] B. Swingle, G. Bentsen, M. Schleier-Smith, and P. Hayden, Measuring the scrambling of quantum information, *Phys. Rev. A* **94**, 040302 (2016).  
 [2] A. Nahum, S. Vijay, and J. Haah, Operator spreading in random unitary circuits, *Phys. Rev. X* **8**, 021014 (2018).  
 [3] V. Khemani, A. Vishwanath, and D. A. Huse, Operator spreading and the emergence of dissipative hydrodynamics under unitary evolution with conservation laws, *Phys. Rev. X* **8**, 031057 (2018).  
 [4] V. Khemani, D. A. Huse, and A. Nahum, Velocity-

dependent lyapunov exponents in many-body quantum, semiclassical, and classical chaos, *Phys. Rev. B* **98**, 144304 (2018).  
 [5] S. Gopalakrishnan, D. A. Huse, V. Khemani, and R. Vasseur, Hydrodynamics of operator spreading and quasiparticle diffusion in interacting integrable systems, *Phys. Rev. B* **98**, 220303 (2018).  
 [6] X.-L. Qi and A. Streicher, Quantum epidemiology: operator growth, thermal effects, and syk, *Journal of High Energy Physics* **2019**, 12 (2019).  
 [7] D. A. Roberts, D. Stanford, and A. Streicher, Operator growth in the syk model, *Journal of High Energy Physics* **2018**, 122 (2018).  
 [8] S. Xu and B. Swingle, Accessing scrambling using matrix product operators, *Nature Physics* **16**, 199 (2020).  
 [9] B. Swingle, Unscrambling the physics of out-of-time-order correlators, *Nature Physics* **14**, 988 (2018).  
 [10] J. M. Deutsch, Quantum statistical mechanics in a closed system, *Phys. Rev. A* **43**, 2046 (1991).  
 [11] M. Srednicki, Chaos and quantum thermalization, *Phys. Rev. E* **50**, 888 (1994).  
 [12] L. D’Alessio, Y. Kafri, A. Polkovnikov, and M. Rigol, From quantum chaos and eigenstate thermalization to statistical mechanics and thermodynamics, *Advances in Physics* **65**, 239 (2016).  
 [13] D. A. Abanin, E. Altman, I. Bloch, and M. Serbyn, Colloquium: Many-body localization, thermalization, and entanglement, *Rev. Mod. Phys.* **91**, 021001 (2019).  
 [14] R. Nandkishore and D. A. Huse, Many-body localization and thermalization in quantum statistical mechanics, *Annual Review of Condensed Matter Physics* **6**, 15 (2015).  
 [15] Y. Sekino and L. Susskind, Fast scramblers, *Journal of High Energy Physics* **2008**, 065 (2008).  
 [16] S. H. Shenker and D. Stanford, Black holes and the butterfly effect, *Journal of High Energy Physics* **2014**, 67 (2014).  
 [17] J. Maldacena, S. H. Shenker, and D. Stanford, A bound on chaos, *Journal of High Energy Physics* **2016**, 106 (2016).  
 [18] A. R. Brown, H. Gharibyan, S. Leichenauer, H. W. Lin, S. Nezami, G. Salton, L. Susskind, B. Swingle, and M. Walter, Quantum gravity in the lab. i. teleportation by size and traversable wormholes, *PRX Quantum* **4**, 010320 (2023).  
 [19] T. Schuster, B. Kobrin, P. Gao, I. Cong, E. T. Khabiboulline, N. M. Linke, M. D. Lukin, C. Monroe, B. Yoshida, and N. Y. Yao, Many-body quantum teleportation via operator spreading in the traversable wormhole protocol, *Phys. Rev. X* **12**, 031013 (2022).  
 [20] T. A. Elsayed, B. Hess, and B. V. Fine, Signatures of chaos in time series generated by many-spin systems at high temperatures, *Phys. Rev. E* **90**, 022910 (2014).  
 [21] D. E. Parker, X. Cao, A. Avdoshkin, T. Scaffidi, and E. Altman, A universal operator growth hypothesis, *Phys. Rev. X* **9**, 041017 (2019).  
 [22] C. Murthy and M. Srednicki, Bounds on chaos from the eigenstate thermalization hypothesis, *Phys. Rev. Lett.* **123**, 230606 (2019).  
 [23] Y. Gu, A. Kitaev, and P. Zhang, A two-way approach to out-of-time-order correlators, *Journal of High Energy Physics* **2022**, 133 (2022).  
 [24] J. L. F. Barbón, E. Rabinovici, R. Shir, and R. Sinha, On the evolution of operator complexity beyond scrambling, *Journal of High Energy Physics* **2019**, 264 (2019).

- [25] E. Rabinovici, A. Sánchez-Garrido, R. Shir, and J. Sonner, Operator complexity: a journey to the edge of krylov space, *Journal of High Energy Physics* **2021**, 62 (2021).
- [26] E. Rabinovici, A. Sánchez-Garrido, R. Shir, and J. Sonner, Krylov complexity from integrability to chaos, *Journal of High Energy Physics* **2022**, 151 (2022).
- [27] A. Avdoshkin and A. Dymarsky, Euclidean operator growth and quantum chaos, *Phys. Rev. Res.* **2**, 043234 (2020).
- [28] A. Dymarsky and M. Smolkin, Krylov complexity in conformal field theory, *Phys. Rev. D* **104**, L081702 (2021).
- [29] A. Avdoshkin, A. Dymarsky, and M. Smolkin, Krylov complexity in quantum field theory, and beyond, [arXiv:2212.14429](https://arxiv.org/abs/2212.14429) (2022).
- [30] S.-K. Jian, B. Swingle, and Z.-Y. Xian, Complexity growth of operators in the syk model and in jt gravity, *Journal of High Energy Physics* **2021**, 14 (2021).
- [31] A. Rubio-Abadal, M. Ippoliti, S. Hollerith, D. Wei, J. Rui, S. L. Sondhi, V. Khemani, C. Gross, and I. Bloch, Floquet prethermalization in a bose-hubbard system, *Phys. Rev. X* **10**, 021044 (2020).
- [32] D. Abanin, W. De Roeck, W. W. Ho, and F. Huveneers, A rigorous theory of many-body prethermalization for periodically driven and closed quantum systems, *Communications in Mathematical Physics* **354**, 809 (2017).
- [33] B. Bhattacharjee, P. Nandy, and T. Pathak, Krylov complexity in large q and double-scaled syk model, *Journal of High Energy Physics* **2023**, 99 (2023).
- [34] B. Bhattacharjee, X. Cao, P. Nandy, and T. Pathak, Krylov complexity in saddle-dominated scrambling, *Journal of High Energy Physics* **2022**, 174 (2022).
- [35] R. Heveling, J. Wang, and J. Gemmer, Numerically probing the universal operator growth hypothesis, *Phys. Rev. E* **106**, 014152 (2022).
- [36] G. Bouch, Complex-time singularity and locality estimates for quantum lattice systems, *Journal of Mathematical Physics* **56**, 123303 (2015).
- [37] X. Cao, A statistical mechanism for operator growth, *Journal of Physics A: Mathematical and Theoretical* **54**, 144001 (2021).
- [38] A. W. Sandvik and J. Kurkijärvi, Quantum monte carlo simulation method for spin systems, *Phys. Rev. B* **43**, 5950 (1991).
- [39] A. W. Sandvik, Computational Studies of Quantum Spin Systems, *AIP Conference Proceedings* **1297**, 135 (2010).
- [40] F. Wang and D. P. Landau, Efficient, multiple-range random walk algorithm to calculate the density of states, *Phys. Rev. Lett.* **86**, 2050 (2001).
- [41] M. Troyer, S. Wessel, and F. Alet, Flat histogram methods for quantum systems: Algorithms to overcome tunneling problems and calculate the free energy, *Phys. Rev. Lett.* **90**, 120201 (2003).
- [42] R. E. Belardinelli, S. Manzi, and V. D. Pereyra, Analysis of the convergence of the  $1/t$  and wang-landau algorithms in the calculation of multidimensional integrals, *Phys. Rev. E* **78**, 067701 (2008).
- [43] Attached supplemental material.
- [44] H. Araki, Gibbs states of a one dimensional quantum lattice, *Communications in Mathematical Physics* **14**, 120 (1969).
- [45] P. Ponte, Z. Papić, F. m. c. Huveneers, and D. A. Abanin, Many-body localization in periodically driven systems, *Phys. Rev. Lett.* **114**, 140401 (2015).
- [46] J. D. Noh, Operator growth in the transverse-field ising spin chain with integrability-breaking longitudinal field, *Phys. Rev. E* **104**, 034112 (2021).
- [47] N. H. Lindner and A. Auerbach, Conductivity of hard core bosons: A paradigm of a bad metal, *Phys. Rev. B* **81**, 054512 (2010).
- [48] S. Bhattacharyya, A. De, S. Gazit, and A. Auerbach, Metallic transport of hard-core bosons, *Phys. Rev. B* **109**, 035117 (2024).
- [49] V. S. Viswanath and G. Müller, Recursion method in quantum spin dynamics: The art of terminating a continued fraction, *Journal of Applied Physics* **67**, 5486 (1990).
- [50] V. Viswanath and G. Müller, *The Recursion Method: Application to Many-Body Dynamics*, Lecture Notes in Physics Monographs (Springer Berlin Heidelberg, 2008).
- [51] I. Khait, S. Gazit, N. Y. Yao, and A. Auerbach, Spin transport of weakly disordered heisenberg chain at infinite temperature, *Phys. Rev. B* **93**, 224205 (2016).
-

# Supplemental Materials: “Stochastic Sampling of Operator Growth Dynamics”

## THE MONTE CARLO ALGORITHM

In this section, we outline our Marko chain Monte Carlo (MCMC) sampling algorithm. We first derive the precise form of the partition function taking into account the re-weighting procedure. Following this, we describe each of the Monte Carlo moves and derive their transition probabilities based on the detailed balance conditions.

We start by deriving Eq. (8) in the paper. Combining  $\mathcal{Z}(\tau = 1/J)$  from Eq. (3) with Eq. (6) in the main text, the partition function becomes:

$$\mathcal{Z}(\tau = 1/J) = \sum_{n=0}^{\infty} \sum_{\mathcal{S}_{2n}} \frac{1}{J^{2n}(2n)!} \prod_{k=0}^{2n-1} (O_{k+1} | \mathcal{L}_{i_k, a_k} | O_k) \quad (\text{S1})$$

where we recall that  $\mathcal{S}_{2n} = \{(i_k, a_k)\}_{k=0}^{2n-1}$  is a sequence of position-type pairs that specify the local Liouvillians  $\mathcal{L}_{i_k, a_k}$ . To proceed, we truncate this partition sum to sequence  $n \geq n_{\max}$ . We also fix the Liouvillian sequences to be of length  $2n_{\max}$ , by inserting  $2n_{\max} - 2n$  factors of the identity Liouvillian  $\mathcal{L}_{0,0}$  in all possible combinations. This procedure however generates duplicate terms which are compensated for by dividing with the combinatorial factor  $\binom{2n_{\max}}{2n_{\max}-2n}$ . This gives us the desired expression of the truncated partition sum:

$$G = \sum_{\mathcal{S}_{2n_{\max}}} \frac{1}{J^{2n}(2n)!} \times \frac{(2n_{\max} - 2n)!(2n)!}{(2n_{\max})!} \prod_{k=0}^{2n_{\max}-1} (O_{k+1} | \mathcal{L}_{i_k, a_k} | O_k). \quad (\text{S2})$$

As mentioned in the main text, the expansion order distribution associated with  $G$  falls typically exponentially on either side of its modal point. In practice, this hinders the sampling of all the  $n_{\max} + 1$  sectors in an ergodic way. To flatten out this distribution, we employ a variant of the Wang-Landau algorithm [S40, S42] that implements a re-weighting procedure. Before explaining our scheme, it is illuminating to rewrite  $G$  using a set of generalized weights  $\{w_n\}$ :

$$G' = \sum_{\mathcal{S}_{2n_{\max}}} w_n \frac{(2n_{\max} - 2n)!(2n)!}{(2n_{\max})!} \prod_{k=0}^{2n_{\max}-1} (O_{k+1} | \mathcal{L}_{i_k, a_k} | O_k) = \sum_n w_n \mu_{2n}. \quad (\text{S3})$$

The weights  $\{w_n\}$  are initialized as  $w_n = 1/(J^{2n}(2n)!)$ . In practice one needs to only keep track of weight ratios between consecutive  $n$  sectors  $w_n/w_{n+1}$ . The reweighting procedure works iteratively. At each step, we take  $N$  samples and determine the number of times  $c_n$  that each sector is visited by the MCMC. We define  $c_n$  as:

$$c_n = \sum_{i=1}^N \delta_{n, n_i}. \quad (\text{S4})$$

For a flat distribution, one expects  $c_n \sim (n_{\max} + 1)/N$ . To bias our distribution in this direction, we update the weights by setting  $w_n \rightarrow w_n N / (c_n (n_{\max} + 1))$ . The corresponding stored weight ratios get updated as:  $w_n/w_{n+1} \rightarrow (w_n/w_{n+1}) \times (c_{n+1}/c_n)$ . This assignment penalizes sectors with  $c_n > (n_{\max} + 1)/N$  by reducing their weight and reinforces weights for sectors with  $c_n < (n_{\max} + 1)/N$ . This procedure is carried out repeatedly until an approximately flat distribution is obtained.

With generalized weights, we need to rescale the counts in Eq. (9) with  $\{w_n\}$  to obtain the moment ratios. Our observables now become:

$$r_n^2 = \frac{\mu_{2n+2}}{\mu_{2n}} = \frac{\langle \delta_{n', n+1} \rangle_{n'}}{\langle \delta_{n', n} \rangle_{n'}} \times \frac{w_n}{w_{n+1}}. \quad (\text{S5})$$

We now move our discussion towards the Monte Carlo moves. The moves are designed to ensure ergodicity while only making local changes to the configuration space. Below, we discuss the three classes of moves: **add-drop**, **swap** and **interact**. For the rest of this section, we will work with a  $d + 1$  dimensional lattice with length  $L$  and  $2n_{\max} + 1$  temporal slices. The temporal axis is pictured in the vertical direction. While the schematic diagrams show the moves on a  $d = 1$  lattice, they generally also apply to higher dimensional cases. We will point out subtleties pertaining to  $d > 1$  dimensions when appropriate.

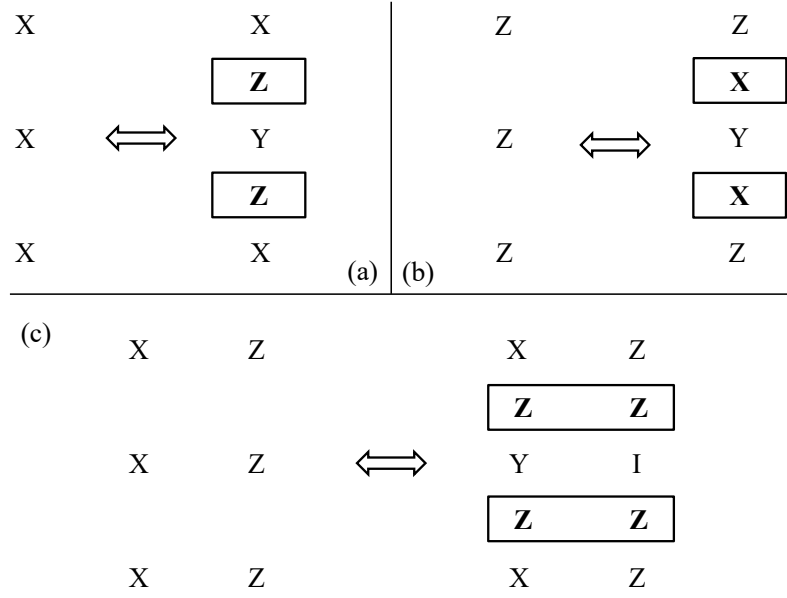


FIG. S1: Illustration of the **add-drop** moves with (a)  $\mathcal{L}_Z$  Liouvillians (b)  $\mathcal{L}_X$  Liouvillians (c)  $\mathcal{L}_{ZZ}$  Liouvillians. The temporal direction is vertical.

### Add Drop

The **add-drop** move is designed to allow transitioning between the different  $n$  sectors by adding and removing a pair of identical local Liouvillians. As illustrated in Fig. S1, the move is defined as follows:

1. Randomly choose a time slice with uniform probability.
2. If the local Liouvillians occupying both sides of the time slice are identical, propose to remove both.
3. Else, if the Liouvillian slots on both sides are unoccupied, randomly choose a site with uniform probability and propose to add a pair of identical Liouvillians onto the unoccupied slots at that site.

We now determine the transition probabilities. Let  $i$  be a configuration in the  $n-1$  sector with the  $(k-1)$ -th and  $k$ -th Liouvillian slots unoccupied. Let  $f$  be a configuration in the  $n$  sector that is identical to  $i$  except with these slots occupied at site  $r$  by Liouvillians  $\mathcal{L}_{r_{k-1}, a_{k-1}} = \mathcal{L}_{r_k, a_k} =: \mathcal{L}_{r, a}$ . The two configurations are thus related by an add-drop move. Based on Eq. (S3), detailed balance imposes the constraint:

$$\frac{T_{i \rightarrow f} A_{i \rightarrow f}}{T_{f \rightarrow i} A_{f \rightarrow i}} = \frac{P_f}{P_i} = \frac{w_n(O_{k-1} | \mathcal{L}_{r, a} | O_k)(O_k | \mathcal{L}_{r, a} | O_{k+1})(2n)(2n-1)}{w_{n-1}(2n_{\max} - 2n + 2)(2n_{\max} - 2n + 1)}. \quad (\text{S6})$$

Here,  $P_i, P_f$  are the respective weights,  $T_{i \rightarrow f}, T_{f \rightarrow i}$  are probabilities to propose the add/drop transitions and  $A_{i \rightarrow f}, A_{f \rightarrow i}$  are the acceptance probabilities for the moves. Now, proposing an **add** operation involves choosing a time slice, followed by choosing a site and then choosing a Liouvillian type; proposing a **drop** amounts to simply choosing a time slice. Therefore the proposition probabilities are

$$T_{i \rightarrow f} = \frac{1}{2n_{\max} + 1} \times \frac{1}{L^d} \times \frac{(O_{k-1} | \mathcal{L}_{r, a} | O_k)(O_k | \mathcal{L}_{r, a} | O_{k+1})}{\sigma}, \quad T_{f \rightarrow i} = \frac{1}{2n_{\max} + 1}. \quad (\text{S7})$$

where we denoted  $\sigma = 4(dJ^2 + (h^X)^2 + (h^Z)^2)$  as the sum of weights of all possible Liouvillians at a site. Therefore, the following ‘‘Metropolis’’ acceptance rates satisfy detailed balance:

$$A_{i \rightarrow f} = \min \left( 1, \frac{w_n L^d \sigma (2n)(2n-1)}{w_{n-1} (2n_{\max} - 2n + 2)(2n_{\max} - 2n + 1)} \right), \quad (\text{S8})$$

$$A_{f \rightarrow i} = \min \left( 1, \frac{w_{n-1} (2n_{\max} - 2n + 2)(2n_{\max} - 2n + 1)}{w_n L^d \sigma (2n)(2n-1)} \right). \quad (\text{S9})$$



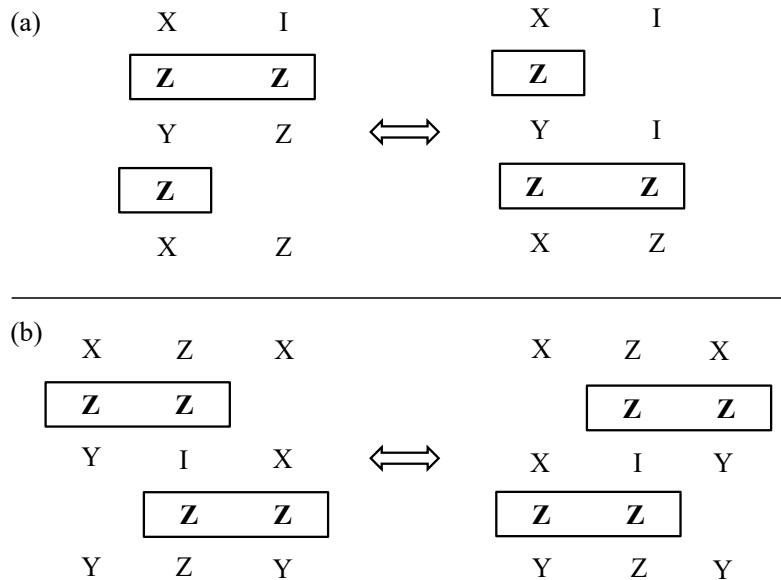


FIG. S2: Illustration of the **swap** move. We show two examples of Liouvillians that commute with each other: (a)  $\mathcal{L}_Z$  and  $\mathcal{L}_{ZZ}$  Liouvillians sharing a site. (b) Two  $\mathcal{L}_{ZZ}$  Liouvillians sharing just one site. In addition to (a) and (b), identical Liouvillians (those of the same kind, on the same site; and along the same axis in case of  $\mathcal{L}_{ZZ}$ ) and those on different sites with no overlap, trivially commute.

### Swap

The **swap** move permutes through different configurations in the same  $n$  sector using the commutation property of Liouvillian pairs, see Fig. Fig. S2 for an illustration. Before discussing the steps, we first define the notion of “ceiling” and “floor”. The ceiling (floor) of a Liouvillian is the temporally closest Liouvillian above (below, respectively) it which doesn’t commute with it. If a non-commuting Liouvillian is lacking, the ceiling/floor is then defined to be the initial/final temporal boundary. Now, the **swap** steps are as follows:

1. Randomly, with uniform probability, choose a Liouvillian.
2. Randomly, with uniform probability, choose a second Liouvillian slot amongst those lying between the ceiling and floor of the first Liouvillian.
3. If the newly chosen slot is empty, remove the Liouvillian from its existing slot and place it in the new slot.
4. Otherwise, that is, if the slot is occupied by another Liouvillian, check whether the ceiling and floor of this second Liouvillian lie at an intermediate temporal index between the indices of the two Liouvillians. If that is not the case, swap the two Liouvillians.

Since the **swap** moves involve no weight change and everything is sampled uniformly, it satisfies detailed balance automatically, that is, with 100% acceptance rate.

### Interact

The **add-drop** move only allows Liouvillians to exist on a site in pairs. This can however miss configurations with an odd number of bond Liouvillians on a site. To enable this we introduce the **interact** move, as illustrated in Fig. S3. It is to be noted that for  $d > 1$ , the two interacting bonds can be along different spatial axes. In such cases, two different  $\mathcal{L}_{ZZ}$  pair configurations can map to the same  $\mathcal{L}_Z$  pair configuration. This needs to be accounted for in detailed balance.

The interaction is implemented as:

1. Randomly choose a time slice with uniform probability.

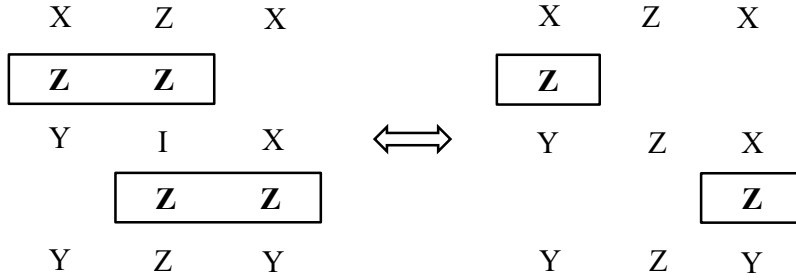


FIG. S3: Illustration of the **interact** move. Two  $\mathcal{L}_{ZZ}$  Liouvillians sharing only one site may “interact” to give a pair of  $\mathcal{L}_Z$  Liouvillians situated on next to nearest neighbour sites.

2. If the Liouvillian on both sides of the time slice are of type  $\mathcal{L}_{ZZ}$  and share exactly one site, check if the shared site has a  $Z$  or  $I$  operator on it. If so, replace the  $\mathcal{L}_{ZZ}$  Liouvillians with  $\mathcal{L}_Z$  Liouvillians as in Fig. S3.
3. If the Liouvillian slots on both sides host  $\mathcal{L}_Z$  Liouvillians placed at next to nearest neighbour sites, check if their common nearest neighbouring site has a  $Z$  or  $I$  operator. If this is the case, replace the  $\mathcal{L}_Z$  Liouvillians with  $\mathcal{L}_{ZZ}$  Liouvillians as in Fig. S3.

Now, we derive the transition probabilities. Let  $i$  be a configuration with  $\mathcal{L}_{ZZ}$  Liouvillians on the  $k - 1$ -th and  $k$ -th time slots sharing a single site  $r$ . Let  $f$  be the configuration related to  $i$  by the **interact** move, hosting two  $\mathcal{L}_Z$  Liouvillians. Now, detailed balance implies:

$$\frac{T_{i \rightarrow f} A_{i \rightarrow f}}{T_{f \rightarrow i} A_{f \rightarrow i}} = \frac{P_f}{P_i} = \frac{(h^Z)^2}{J^2} \quad (\text{S10})$$

where  $P_i, P_f$  are the respective weights,  $T_{i \rightarrow f}, T_{f \rightarrow i}$  are proposition probabilities and  $A_{i \rightarrow f}, A_{f \rightarrow i}$  the acceptance probabilities. We claim that the proposition probabilities are as follows:

$$T_{i \rightarrow f} = \frac{1}{2n_{\max} + 1}, \quad T_{f \rightarrow i} = \frac{1}{(2n_{\max} + 1)\alpha}, \quad (\text{S11})$$

where  $\alpha = 2$  if the  $\mathcal{L}_{ZZ}$  Liouvillians in configuration  $i$  are along different spatial directions (otherwise,  $\alpha = 1$ ). This is because, proposing a  $\mathcal{L}_{ZZ} \rightarrow \mathcal{L}_Z$  **interact** move amounts to choosing a time slice. Meanwhile, to specify a  $\mathcal{L}_Z \rightarrow \mathcal{L}_{ZZ}$  **interact** move, we need choose a time slice, and then pick a common neighboring site among the  $\alpha$  choices. Therefore, the following acceptance rates fulfill detailed balance:

$$A_{i \rightarrow f} = \min\left(1, \frac{(h^Z)^2}{\alpha J^2}\right), \quad A_{f \rightarrow i} = \min\left(1, \frac{\alpha J^2}{(h^Z)^2}\right). \quad (\text{S12})$$

## THE X OPERATOR

The statistical nature of infinite temperature operator growth dynamics in non-integrable systems like the mixed field QIM implies that local operators should typically give rise to the same generic behavior at a large enough order  $n$ . Based on the Operator Growth Hypothesis [S21], one expects local operators to asymptotically grow linearly with the same slope. To check this, we compute the same plots as Fig. 3 but for the  $X$  operator in Fig. S4. We see that for 1D  $\log(n)\Delta r_n$  vs  $n$  again gives us a constant curve  $\log(n)\Delta r_n \simeq 2.2(1)J$ , the same as the  $Z$  operator in the main text. Similarly, in 2D we again get a plot consistent with linear growth with slope  $\simeq 1.26(4)J$ . Another point to note is the non-universal nature of the intermediate plateau in the 2D  $\Delta r_n$  vs  $n$  plot. We see that here the plateau is much narrower than the one for the  $Z$  operator as shown in the main text.

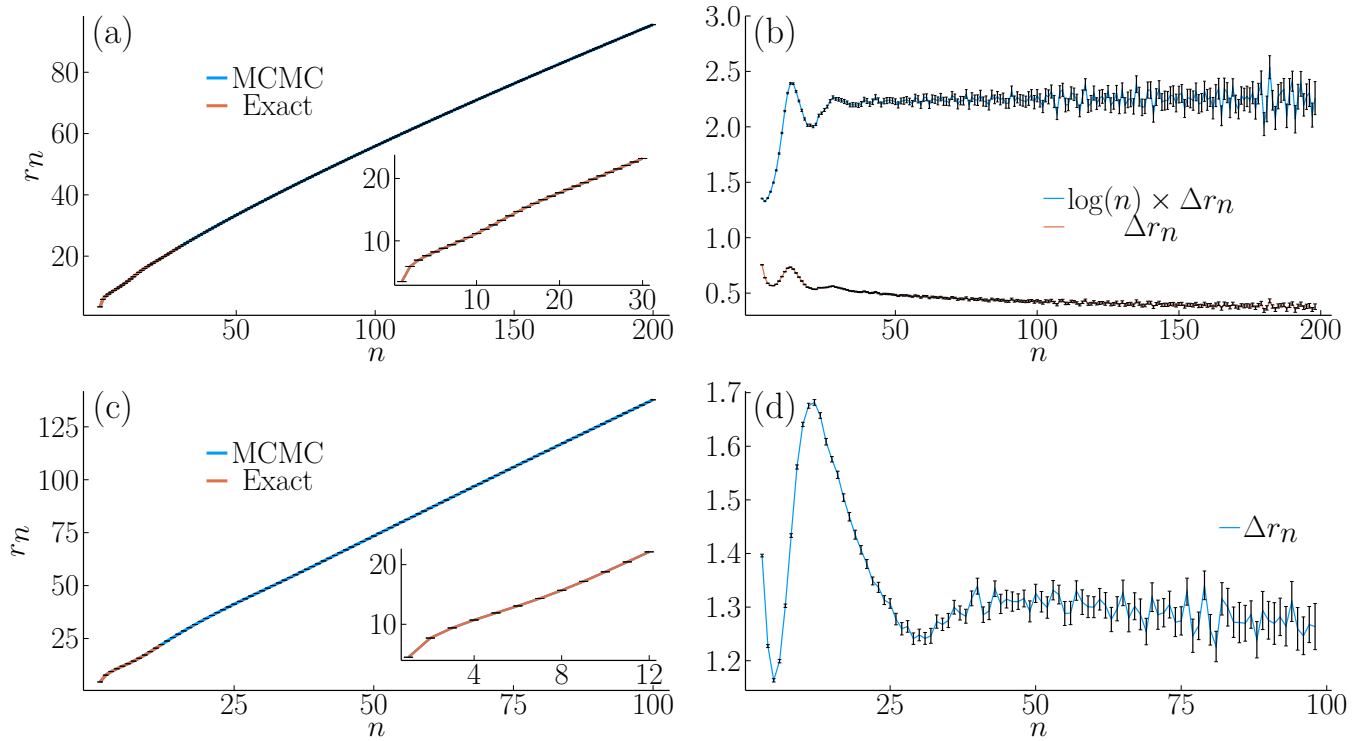


FIG. S4: (a)  $r_n$  vs  $n$  for the  $X$  operator with  $J = h^Z = h^X = 1$  in 1D. The inset focuses in on the first 30 moments, comparing our MCMC with exact numerics. (b)  $\Delta r_n$  and  $\log(n)\Delta r_n$  vs  $n$  for 1D. (c) Same as (a) for 2D. The inset has the first 12 moments. (d)  $\Delta r_n$  vs  $n$  for 2D.

#### ADDITIONAL MOVE FOR THE TFIM LIMIT

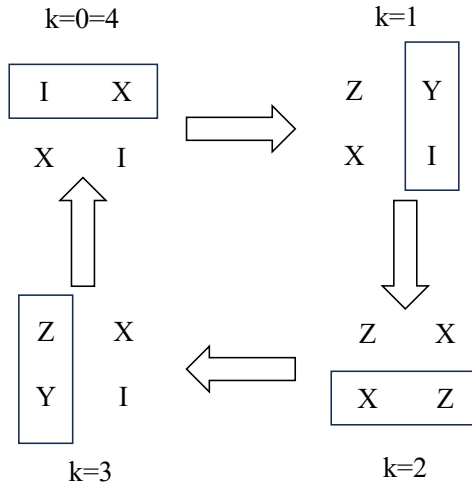


FIG. S5: An example of a configuration in the  $n = 2$  sector that requires the **interact** move to be generated. Temporal slices of the 2D lattice are indexed by  $k$ . The first temporal slice is identical to the last because of the fixed boundary conditions. The  $\mathcal{L}_{ZZ}$  Liouvillians, shown as rectangular boxes, transform local Pauli operators between slices.

In the  $h^Z = 0$  limit, the **interact** move breaks down. This is not a problem in 1D as configurations with an odd number of identical  $\mathcal{L}_{ZZ}$  Liouvillians also require the presence of  $\mathcal{L}_Z$  Liouvillians and thus do not exist in this limit. For  $d > 1$  it is possible for configurations to have an odd number of identical  $\mathcal{L}_{ZZ}$  Liouvillians without  $\mathcal{L}_Z$  Liouvillians. Fig. S5 shows a simple example with  $\mathcal{L}_{ZZ}$  Liouvillians *looping* around a plaquette, satisfying the boundary conditions. Note that each site hosts just one  $\mathcal{L}_{ZZ}$  Liouvillian of a kind. One can generate larger *loops* by removing  $\mathcal{L}_{ZZ}$  pairs on the common edges of overlapping smaller *loops* using **add-drop**.

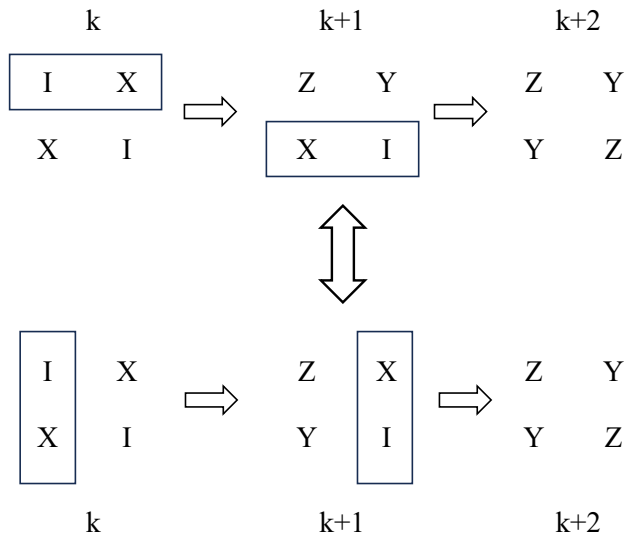


FIG. S6: Section of two configurations connected by the `rotate` move on a 2D lattice.  $k$  corresponds to the temporal index. Note that both configurations have the same temporal boundaries, implying the local nature of the move.

To access this part of the configuration space in absence of `interact` we propose the `rotate` move. Fig. S6 shows that it is possible to rotate two parallel  $\mathcal{L}_{ZZ}$  Liouvillians sharing a plaquette to get another pair of parallel  $\mathcal{L}_{ZZ}$  Liouvillians on the same plaquette while maintaining the same boundaries. Detailed balance for this move should be trivial as the involved configurations have the same weight and the Metropolis acceptance rate is 100%. It can be seen that a combination of `add-drop` and `rotate` can generate the configuration in Fig. S5. We benchmark this move against exact numerics in Fig. S7.

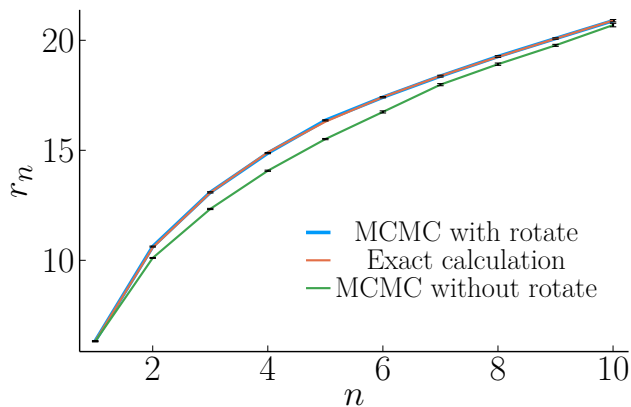


FIG. S7: Comparing our MCMC equipped with and without the `rotate` move against exact computations for the 2D TFIM with the same boundary operator as in Fig. S5.